# Global eigenfunctions of supersonic jets: vortical, acoustic, and thermal components

By M. Karp† and M. J. P. Hack

## 1. Motivation and objectives

Supersonic jets are ubiquitous in many practical applications, including jet engines and rockets. Jet flows are generally unsteady and accompanied by structural vibrations as well as noise. In non-perfectly expanded jets, the phenomenon of jet screech, an intense tone associated with interactions of instability waves and shocks, may place severe limitations on engines due to structural fatigue and significant noise. Understanding the mechanism of unsteadiness may aid in developing quieter and more capable jet engines.

Local stability theory has been commonly applied to perfectly expanded jets since they vary slowly with respect to the axial coordinate, with the exception of the region in the immediate vicinity of the nozzle. The instability mechanism identified by local stability theory is associated with the inflectional shear layer and describes a convectively unstable Kelvin-Helmholtz mode. Several investigators have considered the effects of non-parallelism (e.g. Malik & Chang 2000) and obtained reasonably good agreement with experiments. Nevertheless, these studies excluded the region close to the nozzle from the analysis. Global stability theory avoids any *a priori* assumptions on the base state, thus offering a natural path towards analyzing the role of the nozzle in the instability mechanism.

The first application of global stability analysis to supersonic jets was performed by Nichols & Lele (2011), who investigated a perfectly expanded non-parallel jet; however, they excluded the nozzle from the computational domain. They showed that in line with local stability theory, all global modes were stable and the least stable mode corresponded to an upstream-traveling acoustic mode.

In this research brief, the effect of the nozzle on the instability mechanism is assessed by means of global stability analysis of fully expanded supersonic jets. An additional setup, comprising the velocity field induced by the nozzle without explicit inclusion of the nozzle in the computational domain, allows us to isolate the effect of the nozzle wall on the instability. The momentum potential theory by Doak (1989) is applied to decompose the eigenfunctions obtained from the global stability analysis into vortical, acoustic, and thermal components.

## 2. Methodology

We conduct global stability analyses of axisymmetric supersonics jets, with the aim of assessing the effect of the nozzle on the instability mechanism. Two setups are considered, schematically depicted in Figure 1. The first case, sketched in Figure 1(a), corresponds to a fully expanded jet and includes the nozzle in the computational domain. This setup allows us to assess the effect of the nozzle on the instabilities of a perfectly expanded

† Presently at Technion, Israel.

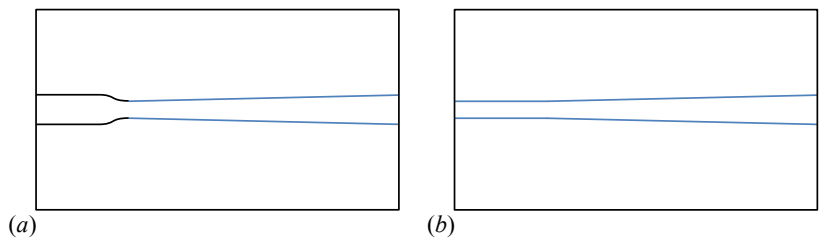


FIGURE 1. Sketches of the two problem setups considered within this work. (a) With nozzle. (b) Without nozzle.

jet. The second case, sketched in Figure 1(b), describes a setup which contains the same expanding jet downstream of the jet exit, with the nozzle being replaced by a parallel jet identical to the jet profile at the nozzle exit. This case allows us to test whether the nozzle wall plays a role in the instability.

In the following subsections, we compute the most unstable eigenfunctions for each of the setups and compare them. The base flows of the linear analyses are obtained as steady laminar solutions of the nonlinear compressible Navier-Stokes equations. In the remainder of this section, the nonlinear equations are presented, followed by the linearized equations and a description of the numerical framework. A summary of the momentum potential theory closes the section.

### 2.1. *Nonlinear compressible Navier-Stokes equations*

The compressible three-dimensional Navier-Stokes equations are considered in conserved form,

$$\frac{\partial \rho}{\partial t} + \frac{\partial m_j}{\partial x_j} = 0, \tag{2.1a}$$

$$\frac{\partial m_i}{\partial t} + \frac{\partial m_i u_j}{\partial x_j} = -\frac{\partial p}{\partial x_i} + \frac{\partial}{\partial x_j}\left[\frac{\mu}{Re}\left(\frac{\partial u_i}{\partial x_j} + \frac{\partial u_j}{\partial x_i} - \frac{2}{3}\frac{\partial u_k}{\partial x_k}\delta_{ij}\right)\right], \tag{2.1b}$$

$$\frac{\partial e}{\partial t} + \frac{\partial (e+p)u_j}{\partial x_j} = \frac{\partial}{\partial x_j}\left(\frac{\mu}{Re\ Pr}\frac{\partial T}{\partial x_j}\right) + \frac{\partial}{\partial x_j}\left[\frac{\mu}{Re}\left(\frac{\partial u_k}{\partial x_j} + \frac{\partial u_j}{\partial x_k} - \frac{2}{3}\frac{\partial u_l}{\partial x_l}\delta_{jk}\right)u_k\right], \tag{2.1c}$$

with the conserved variables given by

$$\boldsymbol{q} \equiv \begin{pmatrix} \rho \\ m_i \\ e \end{pmatrix} = \begin{pmatrix} \rho \\ \rho u_i \\ p/(\gamma-1) + \rho u_k u_k/2 \end{pmatrix}. \tag{2.2}$$

All variables are made non-dimensional by $\rho_e^*$, $a_e^*$, $T_{ref} = (a_e^*)^2/c_p^*$, $p_{ref} = \rho_e^*(a_e^*)^2$, $\mu_e^*$, and $R_e^*$, where $^*$ implies dimensional quantities and the subscript $e$ refers to the nozzle exit. The acoustic Reynolds number is defined as $Re = \rho_e^* a_e^* R_e^*/\mu_e^*$. The velocity components $(u, v, w)$ correspond to velocities along $(x, r, \phi)$, the streamwise, radial, and azimuthal dimensions, respectively.

As mentioned above, the nonlinear equations are used to obtain the laminar base flows for the stability analysis. For the case shown in Figure 1(a), the geometry of the nozzle is represented within the computational domain. The subsonic Mach number inside the

nozzle, $M_{in}$, is calculated based on one-dimensional isentropic flow relations to achieve a given nozzle exit Mach number, $M_e$. Recirculations in the computational domain due to entrainment are avoided by imposing a co-flow with magnitude $1\% M_e$ at the inflow outside of the nozzle. The ambient flow conditions are

$$T_a = T_e \left(1 + \frac{\gamma - 1}{2} M_e^2\right), \quad p_a = \frac{p_e}{r_p}, \tag{2.3}$$

where $r_p$ is the ratio of the nozzle exit pressure and the ambient pressure, and the nozzle exit conditions are $T_e = (\gamma - 1)^{-1}$ and $p_e = \gamma^{-1}$. The wall is assumed isothermal with temperature matching the ambient temperature: $T_w = T_a$. Ambient conditions are imposed at the top of the computational domain, and the quantities at the outflow are extrapolated from inside the domain to avoid streamwise gradients at that region. A power law is assumed for the viscosity, $\mu \sim T^{0.7}$, and the Prandtl number, $Pr = c_p^* \mu^* / \kappa^*$, is assumed to have a constant value of 0.7.

The nozzle in the current study is chosen to yield an exit Mach number of $M_e = 1$. It consists of a convergent part with a length of 3.4, and the ratio of the radii at the inlet and exit is set to 1.5. Thus, the inflow Mach number in the nozzle is $M_{in} = 0.268$. The wall thickness of the nozzle is 0.1, contracting to 0.03 at the lip, with the slope at the outer side of the lip set to 10°. The base flows are obtained for a computational domain of dimensions $L_x = 277$ and $L_r = 200$.

### 2.2. *Linearized compressible Navier-Stokes equations*

The conserved variables are decomposed into a steady base state, denoted by an overbar, and a disturbance, indicated by a prime symbol; i.e.,

$$\boldsymbol{q} = \bar{\boldsymbol{q}}(\boldsymbol{x}) + \boldsymbol{q}'(t, \boldsymbol{x}). \tag{2.4}$$

Substituting the above expression into the governing equations, and retaining only linear terms with respect to the perturbations, yields the linearized compressible three-dimensional Navier-Stokes equations, which can be written in the following form

$$\frac{\partial \boldsymbol{q}'}{\partial t} + \frac{\partial \boldsymbol{F}_j'(\boldsymbol{q}')}{\partial x_j} = 0, \tag{2.5}$$

where $\boldsymbol{F}'$ corresponds to the linearized operator whose explicit expressions can be found in the Appendix. Since the base state is homogeneous in time, the disturbance can be further decomposed as

$$\boldsymbol{q}'(t, \boldsymbol{x}) = \hat{\boldsymbol{q}}(\boldsymbol{x}) \exp(-\mathrm{i}\omega t), \tag{2.6}$$

where $\omega = \omega_r + \mathrm{i}\omega_i$ is the eigenvalue and $\hat{\boldsymbol{q}}(\boldsymbol{x})$ is the eigenfunction. The real part of the eigenvalue gives the disturbance frequency, and the imaginary part gives the growth rate.

Homogeneous Dirichlet boundary conditions are imposed on the perturbations at the inflow, outflow, and radial boundary of the computational domain. The perturbation boundary conditions at the isothermal nozzle wall are vanishing velocity and temperature, with the remaining quantities determined as part of the solution. The computational domain for the calculation of the disturbances is extended upstream to $x = -175$, such that $L_x = 452$ and $L_r = 200$. The eigenmodes are calculated by performing a dynamic mode decomposition (Schmid 2010) of the time series in a part of the computational

domain close to the nozzle exit, thus avoiding effects of the boundaries and the need to use sponge layers.

An additional detail addressed in this subsection concerns the disturbance pressure, required for the momentum potential theory. It is recovered from the disturbance conserved variables using the following relation

$$p' = \left(e' + \frac{1}{2}\bar{u}_i\bar{u}_i\rho' - \bar{u}_i m_i'\right)(\gamma - 1). \tag{2.7}$$

### 2.3. *Numerical framework*

Both nonlinear and linearized equations are consistently implemented in the same computational framework. The spatial discretization uses a fourth-order finite-difference formulation based on summation by parts (Strand 1994). Time integration is facilitated by a fourth-order explicit Runge-Kutta scheme. The solver supports complex geometries via a curvilinear formulation that satisfies geometric conservation properties (Thomas & Lombard 1979). Boundary conditions are weakly enforced via the simultaneous approximation terms (Svärd & Nordström 2014). Capture of the shocks in the nonlinear calculations is achieved by using the artificial bulk viscosity (Kawai & Lele 2008). The reader is referred to Flint & Hack (2018) for a full description of the numerical implementation.

### 2.4. *Doak's decomposition*

The momentum potential theory by Doak (1989) applies a Helmholtz decomposition of the momentum

$$\boldsymbol{m}' = \boldsymbol{B}' - \nabla\psi', \tag{2.8}$$

where $\boldsymbol{B}'$ is the solenoidal field, $\nabla \cdot \boldsymbol{B}' = 0$, and $\psi'$ is the potential, irrotational field. The irrotational field is obtained by applying the divergence to Eq. (2.8) and solving the Poisson equation

$$\nabla^2\psi' = \frac{\partial\rho'}{\partial t}, \tag{2.9}$$

where $\rho'$ is the fluctuating density. The solenoidal field is then recovered using Eq. (2.8). The irrotational field can be further decomposed into acoustic, $\psi_a'$, and thermal, $\psi_t'$, fluctuations by assuming all pressure fluctuations are acoustic. The acoustic part is found by solving the Poisson equation,

$$\nabla^2\psi_a' = \frac{1}{\bar{a}^2}\frac{\partial p'}{\partial t}, \tag{2.10}$$

where $p'$ is the pressure fluctuation. The thermal fluctuations are easily obtained by

$$\psi_t' = \psi' - \psi_a'. \tag{2.11}$$

Utilizing the decomposition introduced in Eq. (2.6) we can write

$$\psi'(t, \boldsymbol{x}) = \hat{\psi}(\boldsymbol{x})\exp(-\mathrm{i}\omega t), \tag{2.12}$$

and similarly for $\boldsymbol{B}'$, $\psi_a'$, and $\psi_t'$, leading to the following equations for the irrotational field

$$\nabla^2\hat{\psi} = -\mathrm{i}\omega\hat{\rho}, \tag{2.13}$$

the acoustic part

$$\nabla^2\hat{\psi}_a = -\frac{\mathrm{i}\omega}{\bar{a}^2}\hat{p}, \tag{2.14}$$

the thermal component

$$\hat{\psi}_t = \hat{\psi} - \hat{\psi}_a, \tag{2.15}$$

and the solenoidal field

$$\hat{\boldsymbol{B}} = \hat{\boldsymbol{m}} + \nabla\hat{\psi}. \tag{2.16}$$

## 3. Laminar base states

In this section, the laminar base states for which the global stability analyses are performed are described. The inflow conditions are set such that the exit Mach number is $M_e = 1$ and the acoustic Reynolds number is $Re = 5000$. Since the laminar base state may be globally unstable, the underlying steady laminar flow is recovered by solving the axisymmetric two-dimensional equations and applying selective frequency damping (Åkervik *et al.* 2006). The computational mesh contains $(N_x, N_r) = (14336, 1536)$ points in the streamwise and radial directions, respectively, clustered around the nozzle lip.

The base flow without the nozzle [Figure 1(b)] is obtained as a steady laminar solution of the axisymmetric two-dimensional equations as well. An initial guess for the solution is obtained by taking the flow field from the case with the nozzle and replacing the nozzle by parallel flow, based on the velocity profile at the nozzle exit. A sponge, located in the region of parallel flow, keeps the parallel flow intact, ensuring maximal similarity to the case with the nozzle.

The base flows are calculated by setting $r_p = 1$, such that the nozzle pressure ratio is 1.89, and the nozzle temperature ratio is 1. The laminar velocity fields are presented in Figure 2, where contours of the Mach number are shown. As detailed above, the base flows with the nozzle [Figure 2(a)] and without the nozzle [Figure 2(b)] are almost identical with the exception of the nozzle region.

The momentum thickness of the shear layer for both considered cases is presented in Figure 3. The distributions are very similar, with differences only in the region close to the nozzle tip ($x \approx 3.5$). Note that a sharp streamwise gradient is present in both base flows at $x \approx 3.5$.

## 4. Linear stability analysis

Our aim is to determine the most unstable eigenmode for each of the base flows described above. The computational mesh contains $N_x \times N_r = 16384 \times 1536$ points along the streamwise and radial directions, respectively, and is obtained by adding points to the left of the computational mesh utilized to obtain the base flow. In the current study, we focus on axisymmetric perturbations, since local stability theory predicts that the mechanism extracting energy from the shear layer is most effective for axisymmetric disturbances.

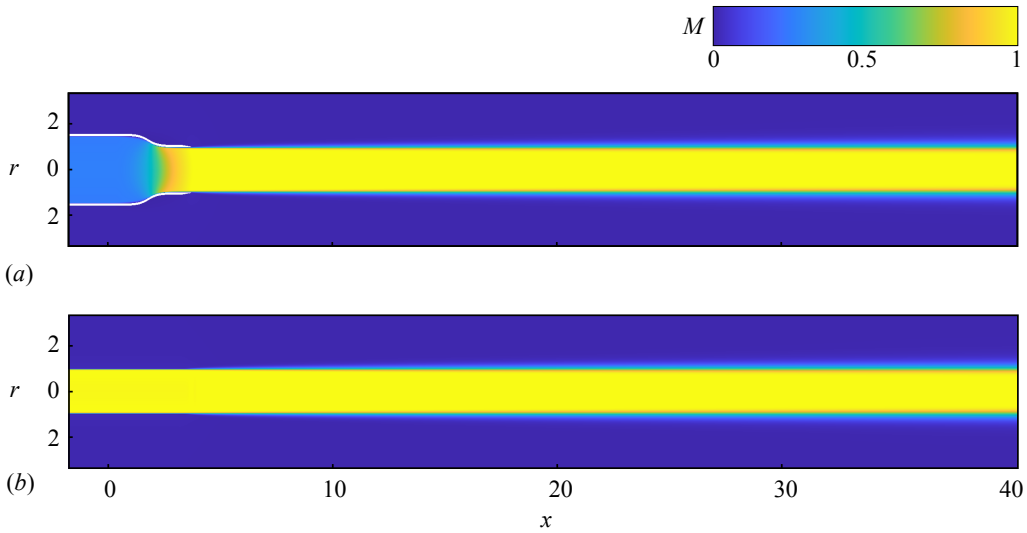


FIGURE 2. Base flow Mach number contours for the cases (a) with the nozzle and (b) without the nozzle. Only the part close to the jet core is shown.

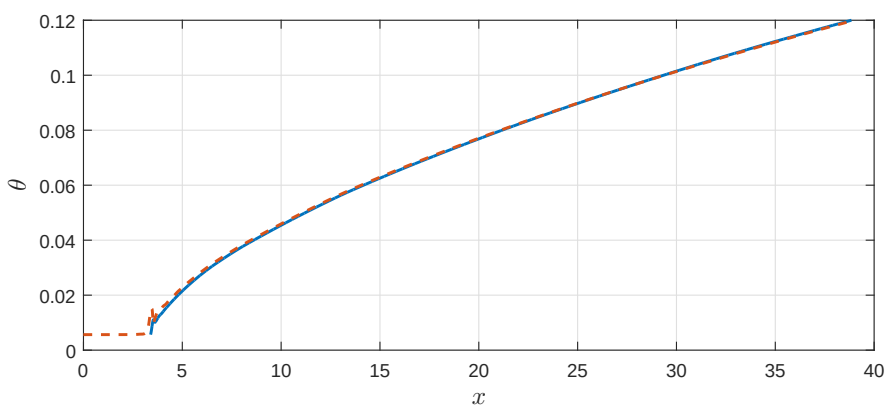


FIGURE 3. Base flow shear-layer momentum thickness for the cases with the nozzle (solid) and without the nozzle (dashed).

The frequency and growth rate of the most unstable eigenmodes for each of the cases are given in Table 1. Both cases with and without the nozzle are globally unstable. As detailed in the review by Huerre & Monkewitz (1990), globally unstable modes are indicative of absolute instability, whereas globally stable modes describe convective instabilities. Thus, the representation of the nozzle within the computational domain introduces an absolute instability, even in absence of shocks. The setup without the nozzle indicates that a global instability is present even without inclusion of the nozzle wall, thus implying that the nozzle wall does not play a role in the instability mechanism.

The eigenfunctions for both cases are presented in Figure 4, with the streamwise momentum component chosen as a representative quantity. The decimal logarithm of the magnitude of the real part is shown in Figure 4(a) for the setup with the nozzle. The peak magnitudes of the eigenfunction are obtained in the shear layer, where downstream

| Case | $\omega_r$ | $\omega_i$ |
|---|---|---|
| With nozzle | 1.72 | 0.03 |
| Without nozzle | 9.11 | 1.97 |

TABLE 1. Frequency ($\omega_r$) and growth rate ($\omega_i$) of the most unstable eigenvalue for the considered cases.

spatial amplification occurs. In the free stream, an upstream-traveling acoustic wave is observed, qualitatively similar to the least stable mode reported by Nichols & Lele (2011). The eigenfunction for the setup without the nozzle is presented in Figure 4(b). The global eigenfunction in that case is focused around the location where the base flow contains a sharp streamwise gradient. The peak magnitudes are found in the shear layer as in the case with the nozzle, although a much smaller streamwise wavenumber is observed for the case without the nozzle. This is because the most amplified wave has a streamwise wavenumber proportional to the shear-layer thickness, and the latter is much smaller at $x \approx 3.5$ compared to $x \approx 10$ (see Figure 3). Acoustic-like emissions, stemming from an apparent source at $x \approx 3.5$, are observed as well, although they have smaller magnitudes compared to the case with the nozzle.

Careful examination of both eigenfunctions enables us to conclude that the flow is absolutely unstable due to the presence of a sharp streamwise gradient in the base flow. The role of the nozzle is limited to generating the velocity field with a sharp streamwise gradient. The inclusion of the nozzle walls leads to a reduction of the instability growth rate due to the constraining effect it has on the eigenfunction.

Performing Doak's decomposition of the above eigenfunction allows us to quantify the vortical, acoustic, and thermal components. The streamwise vortical momentum fluctuations, $B'_x$, obtained from the solenoidal field, are shown in Figure 5(a) for the case with the nozzle. The fluctuations are almost entirely limited to the region of the core, with the peak magnitudes attained in the shear layers. The streamwise component of the gradient of the irrotational field, $\nabla\psi'$, is shown in Figure 5(b). These fluctuations are minimally affected by the jet and have similar wavelengths and magnitudes in the free stream and jet core. Further decomposition of the irrotational field into acoustic and thermal fluctuations is shown in Figures 5(c) and 5(d), respectively. The figure shows that the acoustic part is qualitatively similar to the total potential field, whereas the thermal part is less dominant than the acoustic fluctuations.

The streamwise vortical momentum fluctuations for the case without the nozzle are shown in Figure 6(a). The peak fluctuations are almost entirely limited to the region of the core, as in the previous case. The streamwise component of the gradient of the irrotational field is shown in Figure 6(b). The irrotational component is qualitatively similar to the vortical component; however, some differences are observed between the two. The irrotational field is slightly weaker and contains a wave emitting downstream with an angle of approximately 45° to the streamwise direction. Further decomposition of the irrotational field into acoustic [Figure 6(c)] and thermal [Figure 6(d)] fluctuations indicates that this wave is acoustic. The thermal part is less dominant than the acoustic part, as in the case with the nozzle.

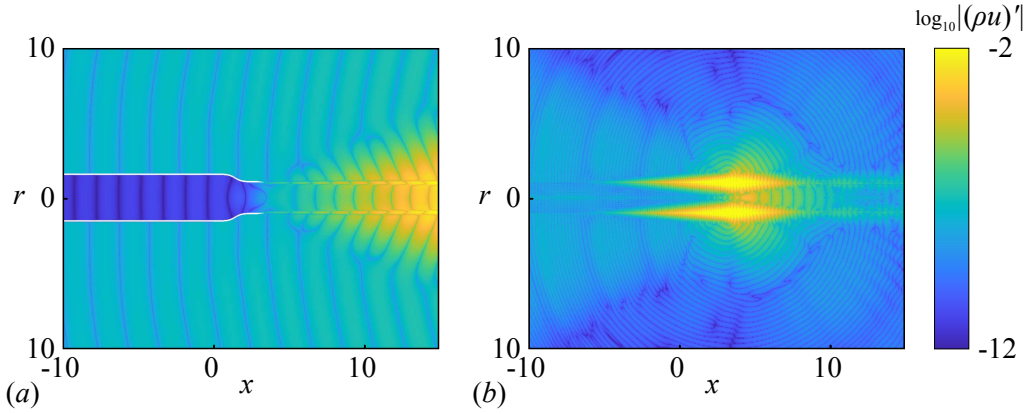


FIGURE 4. Streamwise momentum eigenfunctions for the cases (a) with the nozzle and (b) without the nozzle. The contours correspond to the decimal logarithm of the magnitude of the real part.

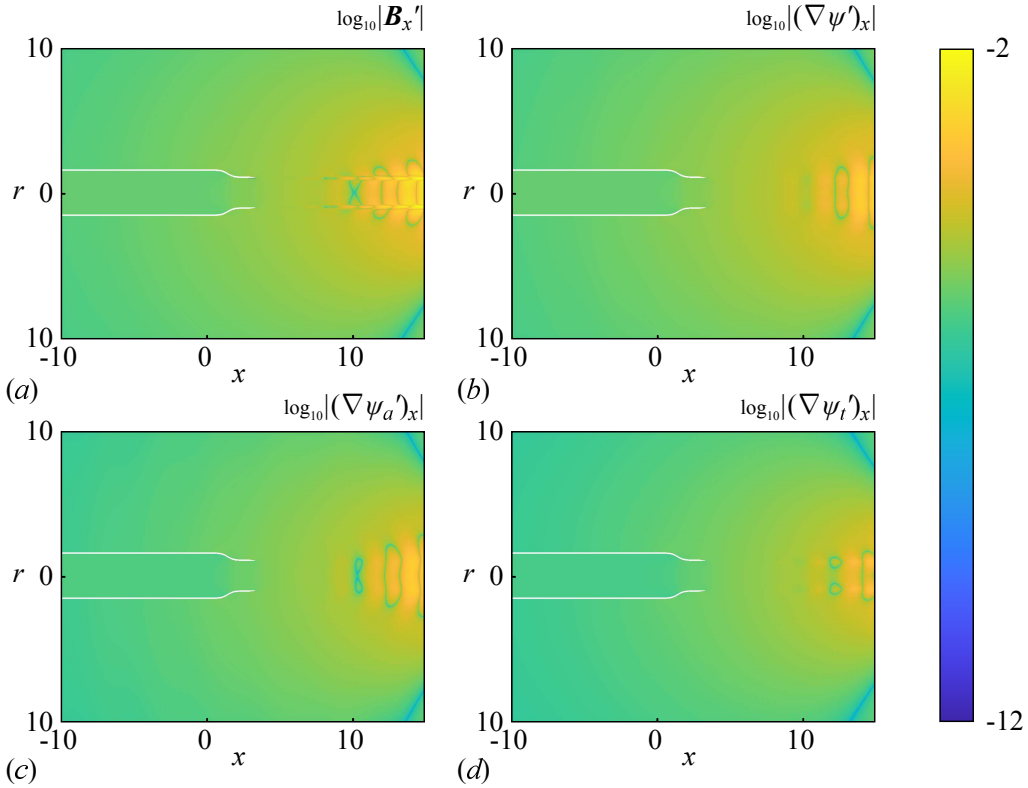


FIGURE 5. Momentum potential theory decomposition of the eigenfunction for the case with the nozzle. The contours correspond to the decimal logarithms of the magnitudes of the real parts. (a) Streamwise vortical momentum fluctuations obtained from the solenoidal part, $\boldsymbol{B}'$. (b) Streamwise gradient of the potential part, $\nabla\psi'$. (c) Streamwise acoustic momentum fluctuations obtained from the gradient of the potential part, $\nabla\psi_a'$. (d) Streamwise thermal momentum fluctuations obtained from the gradient of the potential part, $\nabla\psi_t'$.

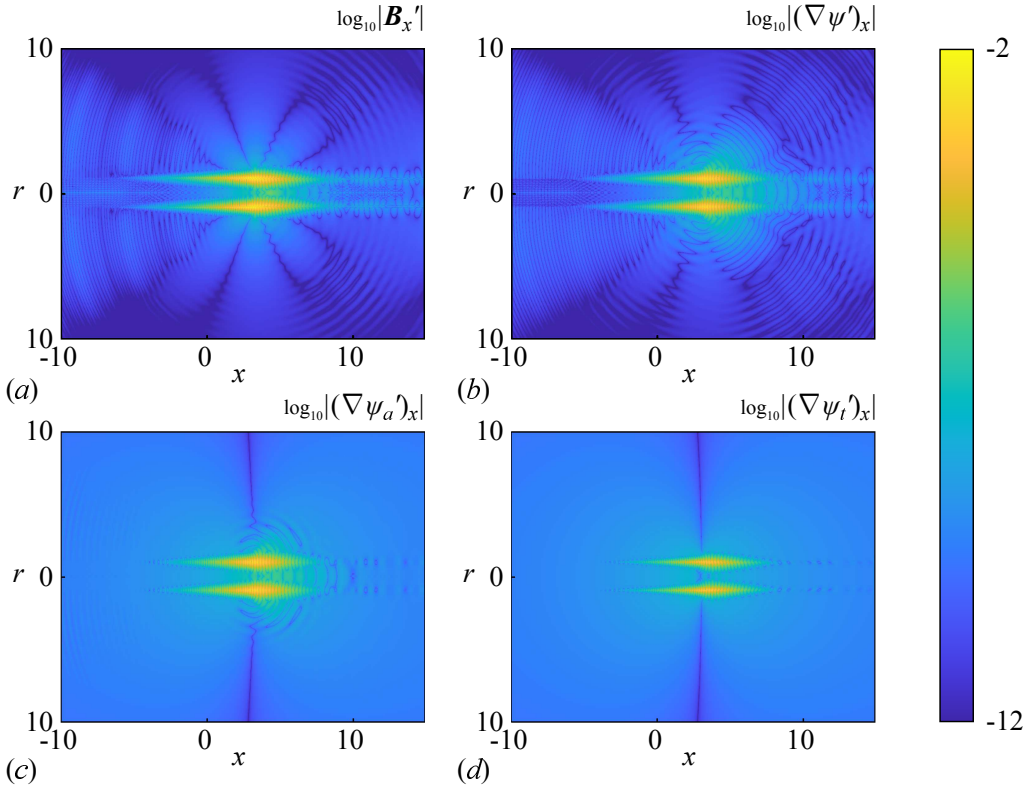


FIGURE 6. Momentum potential theory decomposition of the eigenfunction for the jet without the nozzle. The contours correspond to the decimal logarithms of the magnitudes of the real parts. (a) Streamwise vortical momentum fluctuations obtained from the solenoidal part, $\boldsymbol{B}'$. (b) Streamwise gradient of the potential part, $\nabla\psi'$. (c) Streamwise acoustic momentum fluctuations obtained from the gradient of the potential part, $\nabla\psi_a'$. (d) Streamwise thermal momentum fluctuations obtained from the gradient of the potential part, $\nabla\psi_t'$.

## 5. Conclusions

The effect of the nozzle on the instability mechanism of supersonic jets is assessed by means of global stability analysis. Two setups of fully expanded jets are considered. The first setup corresponds to a jet emanating from a convergent nozzle, with the nozzle represented inside the computational domain. An additional setup, where the nozzle is replaced by a parallel jet, allows us to isolate the effect of the nozzle wall on the instability mechanism.

We found that both base flows are globally unstable, which is indicative of an absolute instability occurring in both cases. The growth rate is larger for the case without the nozzle, for which the eigenfunction is focused in the region where a sharp gradient exists in the base flow. Inclusion of the nozzle walls leads to a reduction of the instability growth rate due to its constraining effect. We concluded that the flow is absolutely unstable due to the presence of a sharp streamwise gradient in the base flow, and the role of the nozzle is limited to the generation of this gradient.

The momentum potential theory presented by Doak (1989) is applied to decompose the eigenfunctions obtained from the global stability analysis into vortical, acoustic, and thermal components. In both setups, the vortical fluctuations are almost entirely limited

to the region of the core, with the peak magnitudes attained in the shear layers. As for the irrotational field, in the case with the nozzle, it is minimally affected by the jet and has similar wavelengths and magnitudes in the free stream and jet core. In the case without the nozzle, the irrotational field is similar to the vortical field, except for a downstream acoustic emission with an angle of approximately 45° to the streamwise direction. In both setups, the acoustic part is qualitatively similar to the total potential field, and the thermal part is less dominant compared to the acoustic fluctuations.

## Acknowledgments

This investigation was funded by the Office of Naval Research under Grant N00014-17-1-2341. The authors acknowledge use of computational resources from the Certainty cluster awarded by the National Science Foundation to CTR.

## Appendix. Linearized compressible Navier-Stokes equations

The linearized compressible Navier-Stokes equations can be written in vector form as

$$\frac{\partial \boldsymbol{q}'}{\partial t} + \frac{\partial \boldsymbol{F}'_j}{\partial x_j} = 0, \tag{5.1}$$

where

$$\boldsymbol{F}'_j \equiv \begin{pmatrix} \bar{\rho} u'_j + \rho' \bar{u}_j \\ \bar{\rho}\bar{u}_i u'_j + \bar{\rho} u'_i \bar{u}_j + \rho' \bar{u}_i \bar{u}_j + p' \delta_{ij} - \sigma'_{ij} \\ \zeta'_j + \iota'_j - \xi'_j \end{pmatrix}, \tag{5.2}$$

and

$$\sigma'_{ij} \equiv \frac{\bar{\mu}}{Re}\left(\frac{\partial u'_i}{\partial x_j} + \frac{\partial u'_j}{\partial x_i} - \frac{2}{3}\frac{\partial u'_k}{\partial x_k}\delta_{ij}\right) + \frac{\mu'}{Re}\left(\frac{\partial \bar{u}_i}{\partial x_j} + \frac{\partial \bar{u}_j}{\partial x_i} - \frac{2}{3}\frac{\partial \bar{u}_k}{\partial x_k}\delta_{ij}\right), \tag{5.3a}$$

$$\zeta'_i \equiv (\bar{p} u'_i + p' \bar{u}_i)\frac{\gamma}{\gamma - 1} + \frac{1}{2}\left(\bar{\rho}\bar{u}_k\bar{u}_k u'_i + 2\bar{\rho}\bar{u}_k u'_k \bar{u}_i + \rho' \bar{u}_k \bar{u}_k \bar{u}_i\right), \tag{5.3b}$$

$$\iota'_i \equiv -\frac{\bar{\mu}}{Re\, Pr}\frac{\partial T'}{\partial x_i} - \frac{\mu'}{Re\, Pr}\frac{\partial \bar{T}}{\partial x_i}, \tag{5.3c}$$

$$\xi'_i \equiv \frac{\bar{\mu}}{Re}\left[\bar{u}_j \frac{\partial u'_j}{\partial x_i} + u'_j \frac{\partial \bar{u}_j}{\partial x_i} + \bar{u}_j \frac{\partial u'_i}{\partial x_j} + u'_j \frac{\partial \bar{u}_i}{\partial x_j} - \frac{2}{3}\left(\bar{u}_j \frac{\partial u'_l}{\partial x_l}\delta_{ij} + u'_j \frac{\partial \bar{u}_l}{\partial x_l}\delta_{ij}\right)\right] + \frac{\mu'}{Re}\left(\bar{u}_j \frac{\partial \bar{u}_j}{\partial x_i} + \bar{u}_j \frac{\partial \bar{u}_i}{\partial x_j} - \frac{2}{3}\bar{u}_j \frac{\partial \bar{u}_l}{\partial x_l}\delta_{ij}\right), \tag{5.3d}$$

with the viscosity perturbation given by

$$\mu' = \frac{\mathrm{d}\bar{\mu}}{\mathrm{d}\bar{T}} T'. \tag{5.4}$$

REFERENCES

Åkervik, E., Brandt, L., Henningson, D. S., Hœpffner, J., Marxen, O. & Schlatter, P. 2006 Steady solutions of the Navier-Stokes equations by selective frequency damping. *Phys. Fluids* **18**, 068102.

Doak, P. 1989 Momentum potential theory of energy flux carried by momentum fluctuations. *J. Sound Vib.* **131**, 67–90.

Flint, T. & Hack, M. J. P. 2018 A computational framework for stability analysis of high-speed flows in complex geometries. *Annual Research Briefs*, Center for Turbulence Research, Stanford University, pp. 221–235.

Huerre, P. & Monkewitz, P. A. 1990 Local and global instabilities in spatially developing flows. *Annu. Rev. Fluid Mech.* **22**, 473–537.

Kawai, S. & Lele, S. K. 2008 Localized artificial diffusivity scheme for discontinuity capturing on curvilinear meshes. *J. Comput. Phys.* **227**, 9498–9526.

Malik, M. R. & Chang, C.-L. 2000 Nonparallel and nonlinear stability of supersonic jet flow. *Comput. Fluids* **29**, 327–365.

Nichols, J. W. & Lele, S. K. 2011 Global modes and transient response of a cold supersonic jet. *J. Fluid Mech.* **669**, 225–241.

Schmid, P. J. 2010 Dynamic mode decomposition of numerical and experimental data. *J. Fluid Mech.* **656**, 5–28.

Strand, B. 1994 Summation by parts for finite difference approximations for $d/dx$. *J. Comput. Phys.* **110**, 47–67.

Svärd, M. & Nordström, J. 2014 Review of summation-by-parts schemes for initial-boundary-value problems. *J. Comput. Phys.* **268**, 17–38.

Thomas, P. D. & Lombard, C. K. 1979 Geometric conservation law and its application to flow computations on moving grids. *AIAA J.* **17**, 1030–1037.